Journal of Power Sources 196 (2011) 7225–7231

Contents lists available at ScienceDirect

Journal of Power Sources

journal homepage: www.elsevier.com/locate/jpowsour

Air side contamination in Solid Oxide Fuel Cell stack testing

J. Andreas Schuler[a,b,*], Christian Gehrig[a], Zacharie Wuillemin[a], Albert J. Schuler[c], Joerg Wochele[c], Christian Ludwig[c,d], Aïcha Hessler-Wyser[b], Jan Van herle[a]

[a] Laboratoire d'énergétique industrielle (LENI), Ecole Polytechnique Fédérale de Lausanne (EPFL), CH-1015 Lausanne, Switzerland
[b] Centre interdisciplinaire de microscopie électronique (CIME), Ecole Polytechnique Fédérale de Lausanne (EPFL), CH-1015 Lausanne, Switzerland
[c] Labor für Bioenergie und Katalyse (LBK), Paul Scherrer Institut (PSI), CH-5232 Villigen PSI, Switzerland
[d] Institut d'ingénierie de l'environnement (ENAC-IIE), Ecole Polytechnique Fédérale de Lausanne (EPFL), CH-1015 Lausanne, Switzerland

ARTICLE INFO

Article history:
Received 14 June 2010
Received in revised form 20 October 2010
Accepted 20 October 2010
Available online 28 October 2010

Keywords:
Solid Oxide Fuel Cell (SOFC)
Contamination
Balance-of-Plant (BoP)
Chromium
Silicon
Sulfur

ABSTRACT

This work aimed to quantify air side contaminants during Solid Oxide Fuel Cell (SOFC) testing in stack configuration. Post-analyses of a long-term test have shown that performance degradation was mainly due to cathode pollutants originated upstream of the cell, therefore their source identification is crucial. The compressed air system, feeding the airflow to the cathode, was investigated by filtering and subsequent chemical analysis of the filters. Hot-air-sampling was redone in situ at the cathode air entry during a new test run to assess the contaminant concentrations in air in SOFC test conditions. In addition, the behavior of SOFC proximal system components, i.e. alloy oxidation, was characterized separately.

Besides the investigation of silicon and sulfur contamination, the present work focused on chromium from high-temperature alloys used in Balance-of-Plant (BoP) components in direct contact with the airflow. Concentrations of volatile Cr-species under SOFC testing conditions were compared to Cr-accumulation on the tested cell as well as to Cr-evaporation rates from BoP alloys, which were individually characterized regarding oxidation behavior. Evaporated Cr quantities were found to saturate the air with Cr-vapors at the cathode air-inlet, as confirmed by the in-situ measurement of volatile species in the hot airflow, and correlate well to accumulated Cr in the cell after long term testing.

The results of this study suggest guidelines to reduce air side contamination from exogenous sources in SOFC stacks.

1. Introduction

In the present context of global warming and increased energy demand, efficiency in energy conversion with minimal environmental impact is a major issue. Direct conversion of chemical energy into electrical energy can be achieved using Fuel Cells. High system efficiency, especially when operated in combined heat and power generation (CHP), and manageable fuel flexibility are expected from Solid Oxide Fuel Cells (SOFCs).

Stationary SOFC-CHP-units have lifetime requirements exceeding 40,000 h. Device longevity over such a time-scale imposes on SOFC components to withstand endogenous degradation effects, and in particular contamination by pollutant species generated in stack and system components, as well as supplied from external sources.

In a previous study, a 200 cm^2 anode-supported cell was tested in repeat-element configuration over 1900 h at 800 °C, showing a degradation rate of 1% kh^{-1}, on a dedicated test bench, allowing locally-resolved studies of performance degradation. Localized X-ray fluorescence (XRF) and scanning/transmission electron microscopy–energy dispersive X-ray spectroscopy (SEM/TEM–EDS) post-test investigations, combined with impedance spectroscopy deconvolution, allowed to pinpoint the origin of local performance degradation, i.e. mainly pollution contamination of the cathode by chromium (Cr), silicon (Si) and sulfur (S). The distribution of impurities on the cathode surface indicated SOFC proximal system components, located upstream the airflow, to be at the origin of volatile contaminants [1,2].

Contamination effects on the durability of SOFC during stack testing were revealed by numerous authors [3–7]. Repeat-element compounds such as metallic interconnects (MICs) are known as possible cathode pollutant sources [8]. Balance-of-Plant (BoP) elements can generate additional contamination [9]. Finally the quality of laboratory air has been mentioned to act on cathode performance [6,10]. However, localization and quantification of air side contaminants is generally insufficient in SOFC testing to ensure controlled operating environments and thereby isolate the studied processes from overlapping effects complicating the interpretation of results.

* Corresponding author at: EPFL-IGM-LENI, Station 9, Ch-1015 Lausanne, Switzerland. Tel.: +41 21 693 4827; fax: +41 21 693 3502.
E-mail address: andreas.schuler@epfl.ch (J.A. Schuler).

0378-7753/$ – see front matter © 2010 Elsevier B.V. All rights reserved.
doi:10.1016/j.jpowsour.2010.10.058

In the present work, the behavior of SOFC proximal system components, especially the oxidation behavior of BoP alloys, is related to identification and quantification of major pollutant species in post-test studies, as well as to *in situ* measurements of contaminant concentrations on the air side of a SOFC stack.

2. Methods

This work presents a three-level analysis of air side contaminations in SOFC testing. Indeed, as illustrated in Fig. 1, contaminants vehicled by the airflow were sampled at different locations in the test bench, i.e. by filtering the compressed air at ambient temperature, sampling the hot air at stack temperature and by analyzing contaminant accumulation in the cathode from post-test experiments. Moreover, focus is given on Cr-containing heat-resistant alloys from the BoP part of the test bench, which are in contact with the hot air flow, and from which evaporation of contaminant species is expected.

3. Experimental

Samples for post-test analyses were taken from an anode-supported repeat-element, including a composite strontium doped lanthanum manganite (LSM)–yttria stabilized zirconia (YSZ) cathode, a strontium doped lanthanum cobaltite (LSC) current collection layer (CCL) and a gas diffusion layer (GDL) made of *SOFConnex*™, which has been tested over 1900 h at 800 °C [2].

The samples were immersed in hot nitric acid to dissolve perovskite cathode layers. The solution was analyzed for Cr-content with a *PerkinElmer-AAnalyst400* (Winlab32 software) atomic absorption spectrometer (AAS), calibrated with standards. After dissolution, zirconia remnants were observed both by XRF, performed on a *Fischer Xan* system and equipped with *WinFam* software, and with a *FEI*-SEM coupled to an EDS-analyzer with a silicon-drift detector from *Oxford Instruments* combined to *Inca* software.

The hot gas sampling was performed using an adapted version of the liquid quench method described by Koebel and Elsener [11]. This was done by pumping the gas during 12 h through a capillary, placed at the air-inlet localization of the cathode, at a sampling flow rate of 1 l min^{-1} from a 20 l min^{-1} 770 °C airflow. Volatile contaminants, present in the hot air, were condensated in an acidic solution, which was analyzed for Cr, Si and S contents on a *PerkinElmer-Optima3300DV* inductively coupled plasma optical emission spectrometer (ICP-OES), calibrated with standards.

The quality of laboratory air was analyzed by SEM–EDS observations of sub-micron syringe filters placed in the compressed air stream during several days at a flow rate of 15 l min^{-1}. The air is dehumidified at 3 °C under 10 bar pressure and its water content is confirmed as 5% relative humidity (RH) at 25 °C with a hygrometer, type *MIK 3000* from *Refco*.

Oxidation behavior of BoP alloys, including austenitic steels, grades 1.4849, 1.4828 and Incoloy 800, was characterized by SEM–EDS measurements on surfaces and polished cross-sections after oxidizing alloy samples at 800 °C for different durations.

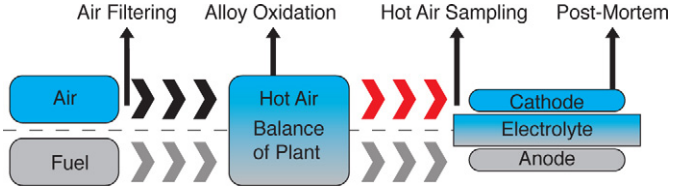

Fig. 1. Schematic drawing of SOFC gas supply. Focus is here on the air-side: the laboratory air stems from a compressed air system; heat-exchangers and tubing elements from the BoP feed the cathode with hot air; hot air sampling is done at the cathode air-inlet; post-test analysis of these regions is mainly done by SEM/EDS observations.

4. Approach

Under oxidizing conditions, Cr-containing high temperature alloys form chromium rich oxide scales on their surface, i.e. mainly Cr_2O_3 chromia and $(Cr,Mn)_3O_4$ spinel phases [12,13]. When exposed to flowing gases, the oxide scale growth is dictated by the mass transfer in the gas boundary layer as well as by the oxidation behavior of the considered alloy [14,15]. In stagnant atmosphere, the oxide scale growth follows a parabolic law according to Wagner's theory of oxidation: dominated by diffusion, it is given by [16–18]:

$$\frac{dX}{dt} = \frac{k_p}{X}; \quad X = \sqrt{2k_p t} \tag{1}$$

where X [cm] is the scale thickness, k_p [cm^2 s^{-1}] is the parabolic oxidation constant, evaluated from experiments in stagnant air, and t [s] the time.

When exposed to flowing gases, the Wagner's parabolic growth rate can be corrected [15,19] by an evaporation factor k_{ev} [cm s^{-1}] which depends locally on the mass transfer properties of the flow, on the difference between the partial pressure of the evaporated species at the oxide scale surface and the one in the gas stream, and consequently on the thermodynamic equilibrium of the vaporization reaction:

$$\frac{dX}{dt} = \frac{k_p}{X} - k_{ev} \tag{2}$$

When the oxide scale growth reaches a steady state, the above equation becomes

$$\frac{k_p}{X_{SS}} = k_{ev} \tag{3}$$

where X_{SS} [cm] is the steady state thickness, determined from samples exposed to flowing gases. The steady-state Cr evaporation rate J_{Cr} [g cm^{-2} s^{-1}] from an oxidized alloy in a non-saturated gas can thus be estimated from thickness measurements using the following equation:

$$J_{Cr} = \frac{3M_O \rho_{Cr_2O_3}}{M_{Cr_2O_3}} \times \frac{k_p}{X_{SS}} \tag{4}$$

where $M_{Cr_2O_3}$ [g mol^{-1}] is the molar mass of chromia and M_O the one for oxygen; $\rho_{Cr_2O_3}$ [g cm^{-3}] is the density of chromia, which equals 5.2 g cm^{-3}.

Volatile Cr species – CrO_3 in dry air and both CrO_3/$CrO_2(OH)_2$ in humid air – evaporate from Cr-containing oxide scales at high temperature. By increasing the water vapor concentration in air, the oxyhydroxide $CrO_2(OH)_2$ species becomes dominant and its concentration increases [20–22]. Cr^{6+} gaseous species are generated according to the following oxidation equations:

$$Cr_2O_3(s) + 3/2O_2(g) \leftrightarrow 2CrO_3(g) \tag{5}$$

$$Cr_2O_3(s) + 3/2O_2(g) + 2H_2O(g) \leftrightarrow 2CrO_2(OH)_2(g) \tag{6}$$

Along the flow through the different BoP components, the gas stream becomes progressively saturated by the evaporated species, reaching possibly the maximal saturation (i.e. the equilibrium partial pressure) for the conditions existing at the cathode air-inlet of the SOFC.

Considerable disagreement is found in literature for the estimation of equilibrium partial pressures [23]. The present work uses data from Wuillemin [24], who extracted thermodynamic data for both Cr-vapor species from the literature.

For CrO_3, the equilibrium partial pressure p_{CrO_3} can be calculated [24], using an equilibrium constant, K_{CrO_3}, fitted on data from

Ebbinghaus [20], which is consistent with results from Gindorf et al. [21]:

$$p_{CrO_3} = K_{CrO_3} \times p_{O_2}^{3/4} \quad (7)$$

$$\log K_{CrO_3} = -12235.38 \times T^{-1} + 3.01 \quad (8)$$

where p_{O_2} [atm] is the oxygen partial pressure and T [K] the temperature. For the oxyhydroxide species $CrO_2(OH)_2$ data from Stanislowski et al. [23], which is in relatively good agreement with those from Opila et al. [14], was used to determine the equilibrium constant [24]:

$$p_{CrO_2(OH)_2} = K_{CrO_2(OH)_2} \times p_{H_2O} \times p_{O_2}^{3/4} \quad (9)$$

$$\log K_{CrO_2(OH)_2} = -2978.43 \times T^{-1} - 1.96 \quad (10)$$

In the following analyses, the experimentally determined amount of Cr-vapors transported in the air stream is compared to the values that could be evaluated using the non-saturation hypothesis (Eq. (4)) and the ones given by thermodynamic equilibrium calculations (Eqs. (7) and (9)).

5. Results and discussion

5.1. Cr contamination

Accumulations of Cr, on the air side of the cell tested over 1900 h, were determined using AAS by measuring Cr-concentrations from post-test samples of the cell taken at different positions along the air-flow. An average value of 35 μg Cr per cm^2 of active area was found in cathode and CCL layers of the repeat-element. This corresponded to a total Cr accumulation of 38 mg for the 200 cm^2 cell, including cathode, CCL and GDL, taking into account the total surface exposed to the airflow and assuming that all Cr entering the cathode compartment is trapped therein [1,2].

Cr-contamination stemming from the MIC was avoided in this test by an effective protective coating [2]. Accumulation of Cr was mainly observed in the air-inlet regions of the cathode, suggesting Cr-contamination from upstream system components. Knowing the surface area of BoP alloys exposed to the hot air-flux (784 cm^2), the total Cr accumulation would correspond to an average Cr evaporation rate from BoP alloys of 7×10^{-11} kg m^{-2} s^{-1}.

Volatile Cr quantification in the hot air flux was enabled by hot air *in situ* sampling followed by chemical analysis. A concentration of 12 ppb (μg m^{-3}) volatile Cr in the hot air flux was established, which would correspond to an accumulation of 28 mg Cr in the cell for 1900 h of operation. Knowing the air-flux rate and the exposed alloy surface, one obtains an evaporation rate of 5×10^{-11} kg m^{-2} s^{-1}. Both Cr-accumulation and evaporation rate are therefore well within the same order of magnitude.

Cr evaporation from BoP alloys exposed to the hot air flux was further estimated from oxidation experiments performed on metal coupons. A SEM picture of a polished cross-section of an Incoloy 800 sample oxidized at 800 °C over 500 h is given in Fig. 2.

The layered structure includes, from bottom to top, the base alloy (light grey) with alumina Al_2O_3 inclusions (dark spots), a silicon-rich sub-scale layer (dark) and a Cr,Mn-containing oxide scale (dark grey). A scale thickness X = 3.5 μm is measured; the thickness evolution with time, for all three alloys, is reported in Fig. 3.

As BoP alloys from the test bench had been operated for several kh before this work, steady-state thicknesses X_{SS} at longer oxidation times were extrapolated from these results, and are reported in Table 1. The growth rates k_p and the evaporation rates J_{Cr} were calculated, by making the hypothesis of non-saturation of the air by Cr-vapor species (Eq. (4)), and are consistent with results from the literature [22,23].

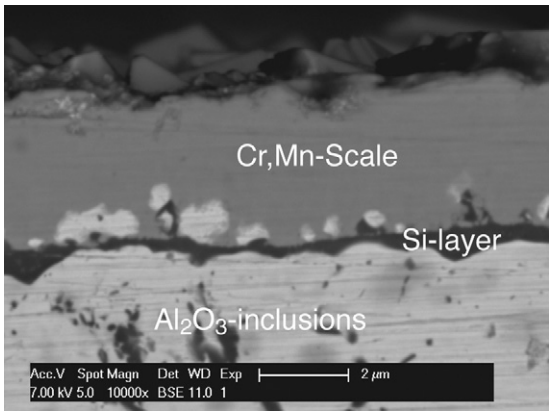

Fig. 2. Cr,Mn-containing oxide scale (dark grey) formed on Incoloy 800 alloy (light grey) after 500 h oxidation at 800 °C observed by SEM on a polished cross-section. A continuous Si-rich sub-scale layer appears for this oxidation time (dark phase).

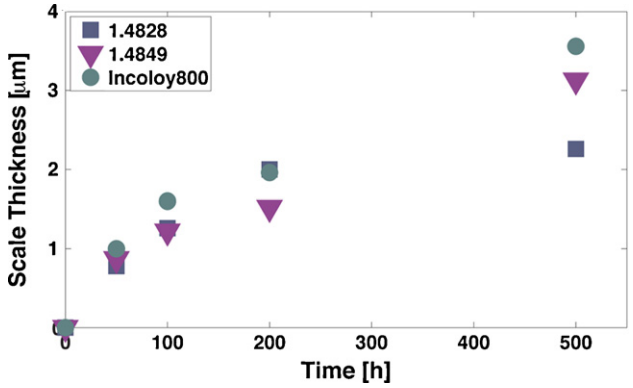

Fig. 3. Oxide scale thickness evolution with time for 1.4828, 1.4849 and Incoloy 800 alloys. Steady-state thickness of 2.2, 5.1 and 4.2 μm, respectively for these alloys, result from scale thickness extrapolation at longer oxidation times.

From this data, a mean evaporation rate was calculated to 13×10^{-11} kg m^{-2} s^{-1} for the exposed alloy surfaces. However, this evaluation, using the non-saturation hypothesis, over-estimates Cr-evaporation. Indeed, thermodynamic equilibrium calculations give saturation pressures of 6×10^{-10} and 8×10^{-9} (atm) for CrO_3 and $CrO_2(OH)_2$, respectively, at the cathode air-inlet. This would correspond to a Cr-evaporation rate of 4.3×10^{-11} kg m^{-2} s^{-1}. In other words, Cr-containing BoP components saturate the hot air with volatile Cr-species.

As filtering the compressed air before the hot air zone (analyzing air-filters before the BoP) revealed no presence of Cr, Cr-evaporation from BoP alloys should equal Cr-concentrations in the hot air flux as well as Cr-accumulation in the cell. Indeed, the amount of Cr was found to be in the same order of magnitude for all three analysis-locations; this result is graphically summarized in Fig. 4.

A correlation between Cr content in the cathode (18 μg cm^{-2} for cathode and CCL for 1 kh) and degradation (1% kh^{-1}) can be done, neglecting other contamination effects similar to other stud-

Table 1
Steady-state oxide scale thickness, parabolic growth rates and corresponding evaporation rates, calculated from the oxidation study of grades 1.4828, 1.4849 and Incoloy 800 alloys.

	1.4828	1.4849	Incoloy 800
Scale thickness, X_{SS} [μm]	2.2	5.1	4.2
Growth rate, k_p [cm^2 s^{-1}] × 10^{-14}	1.3	2.8	3.6
Evaporation rate, J_{Cr} [kg m^{-2} s^{-1}] × 10^{-10}	1	0.9	1.4

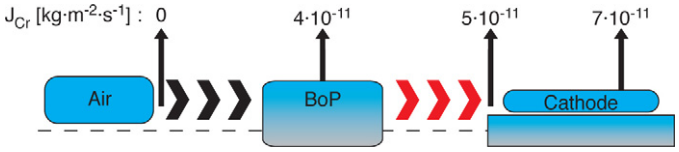

Fig. 4. Hot air *in situ* sampling allowed direct access to the concentration of volatile Cr-species. The quantity of Cr in air can be related to Cr-evaporation from the source and to Cr-accumulation as cathode poison. Cr evaporation rates calculated from oxidation studies of BoP alloys, hot air sampling and post-test analyses all correlate well.

ies. Indeed, Stanislowski et al. [25] report 4 μg cm^{-2} for degradation rates of 1% kh^{-1}, considering that the evaporated Cr-content from a MIC, of equal surface compared to the cell, is totally trapped by the latter. The study of Menzler et al. [26], who correlated degradation rates to Cr-accumulation in cathodes for a dozen stack-tests, mentions 15 μg cm^{-2} for tests with less than 1.5% kh^{-1} degradation (averaged value). However, previous studies [2,24] pointed out the important difference between global and local degradation rates of a repeat-element. Local distribution of pollutant species [1] could be related to local degradation rates, whereas the low-degraded areas were mainly free of contamination.

5.2. Other contamination

Scale composition is however not only limited to chromia. During oxidation, the scale composition evolves from a chromia-rich structure to a Cr/Mn-containing spinel type phase, reducing Cr-evaporation.

Fig. 5 shows the surface structure of a chromia oxide scale, with characteristic hexagonal-shaped plates, observed after 50 h oxidation on grade 1.4828 alloy. At longer oxidation times, as the Mn-content in the oxide scale increases, a structure transition from chromia plates into pyramidal spinel structures is observed. Fig. 6 illustrates a surface view of 1.4828 alloy after 500 h oxidation, with a coarsened structure.

Elemental analyses of oxide scales were performed by EDS surface scans adjusting acceleration potential to minimize signal contribution from the sub-scale bulk alloy. The evolution of the oxide scale composition for the studied alloys is reported in Fig. 7. For all three alloys, the Mn-content increases with time and stabilizes.

The oxide scales are tending towards the following compositions: $(Cr_{0.7}Mn_{0.3})_3O_4$, $(Cr_{0.8}Mn_{0.2})_3O_4$ and $(Cr_{0.75}Mn_{0.25})_3O_4$, for grade 1.4828, 1.4849 and Incoloy 800 alloys, respectively. In the case of Incoloy 800, contrary to the predicted formation of internal TiO_2 sub-scale precipitates, Ti was found in

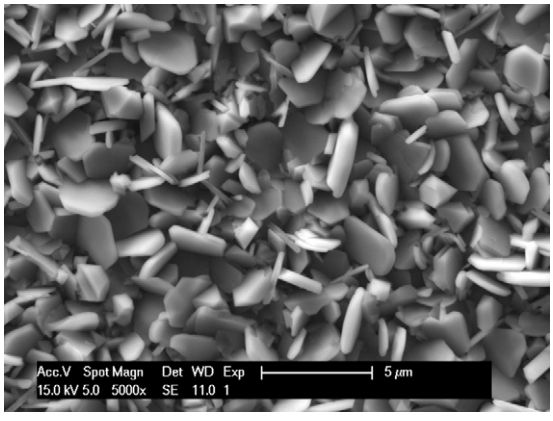

Fig. 5. Hexagonal-shaped crystal plates, characteristic of a chromia scale, are observed on grade 1.4828 alloy surface after 50 h oxidation at 800 °C.

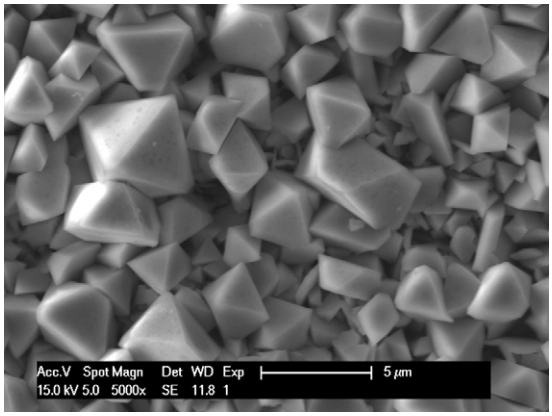

Fig. 6. Surface view of grade 1.4828 alloy after 500 h oxidation at 800 °C showing pyramidal-shaped crystals characteristic for Cr,Mn-spinels.

the scale, suggesting formation of $(Cr,Mn)_2Ti_3O_4$ on the surface [22].

The oxide scales on all three alloys presented a tendency to delaminate; simple manipulations of oxidized alloy samples lead to spallation of the scale. Fig. 8 shows a low magnification view of an alloy surface with delaminated scale. Nevertheless, delaminated regions allowed EDS analyses on both scale remnants (dark regions) and sub-scale surfaces (light grey regions).

In the latter, high concentrations of Si are observed, as shown in Table 2. Si-rich sub-scale phases are known to enhance scale delamination upon thermal variations, as the thermal expansion coefficient (TEC) is different for scale ($Cr_2O_3 \sim 8.5 \times 10^{-6}\,K^{-1}$) and sub-scale layers ($SiO_2 \sim 0.5 \times 10^{-6}\,K^{-1}$; alloy $\sim 15 \times 10^{-6}\,K^{-1}$) [27]. The sub-scale phase is expected to be amorphous SiO_2, as reported by Bauer et al. [27]; the absence of grain-boundaries (fast diffusion) should lead to slow-growing chromia layers.

As scale delamination exposes Si-rich sub-scale alloy surfaces to the hot air flux in BoP components, high temperature alloys are supposed to be sources of Si-contamination in SOFC testing. Such observations were done before by Kaus et al. [28], where a 1.77% Si-containing furnace tube material was a source of Si poisoning for oxygen membranes. Si-rich sub-scale phases result from internal oxidation of Si and segregation of Si-phases at the interface [22]. Si-containing volatile species evaporate from SiO_2 in the form of hydroxides and oxyhydroxides as described in the literature [14,29,30], according mainly to the following reaction, at temperature ranges of 800–1000 °C.

$$SiO_2 + 2H_2O(g) \leftrightarrow Si(OH)_4(g) \quad (11)$$

Nevertheless, Kaus et al. reported the difficulty of Si identification by EDS in strontium (Sr) containing materials due to the overlap of Sr Lα and Si Kα X-ray emission lines, which are at 1.806 and 1.740 keV, respectively.

In this study, the post-test acidic dissolution of strontium allowed bypassing the difficulty of Si identification by EDS. Fig. 9 shows a characteristic pattern of Si-distribution within the zirconia remnants of the cathode, following the airflow, which allows to distinguish between Si as bulk impurity [31–34] and exogenous Si as pollutant; its source is located upstream of the airflow [1,2].

Table 2
Si concentration [% at] measured by EDS scans of sub-scale layers on alloy surface regions with delaminated oxide scales.

Time [h]	50	100	200	500
1.4828	3.99	3.96	3.91	4.15
1.4849	nd	nd	3.64	4.64
Incoloy 800	nd	nd	4.98	3.82

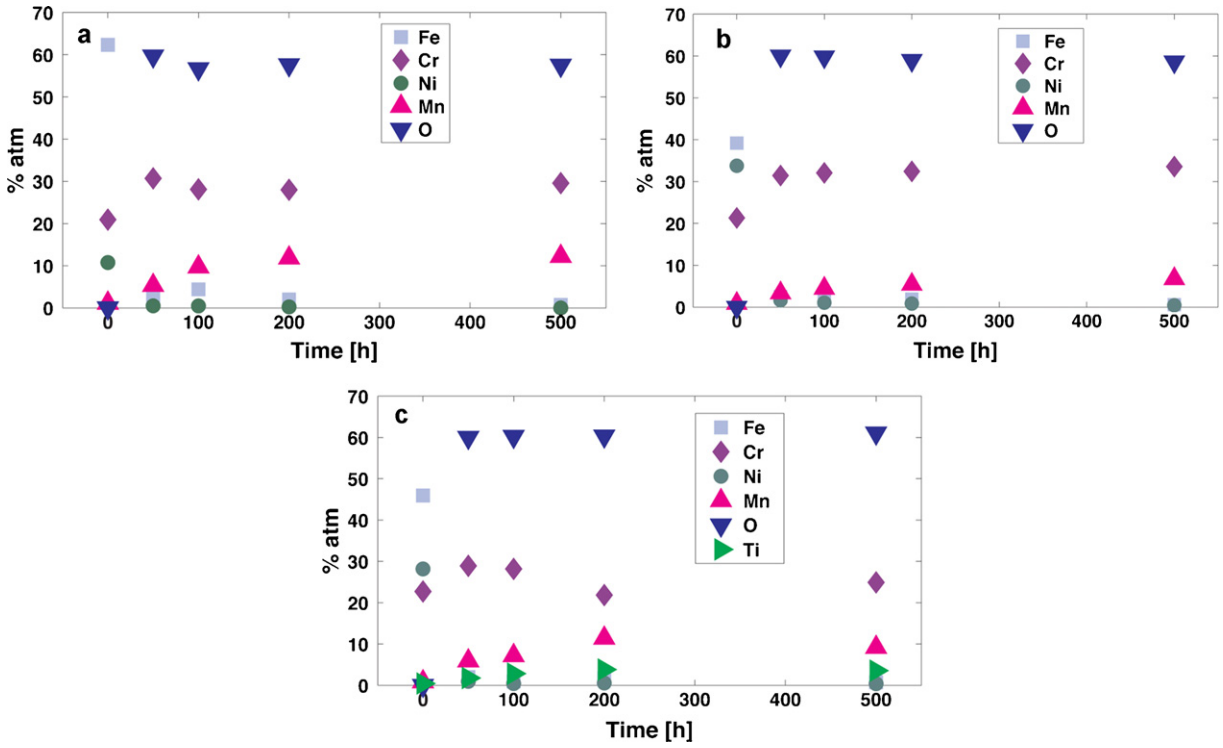

Fig. 7. Evolution with time of oxide scale composition of grade (a) 1.4828, (b) 1.4849 and (c) Incoloy 800 alloys; the scale tends towards $(Cr_{0.7}Mn_{0.3})_3O_4$, $(Cr_{0.8}Mn_{0.2})_3O_4$ and $(Cr_{0.75}Mn_{0.25})_3O_4$, spinel-type compositions, respectively.

As expected after post-test observation, volatile Si species were also revealed by the analyses of hot air samples: 34 $\mu g\,m^{-3}$ Si was measured. Such an amount of Si would correspond to a Si accumulation in the cell of 70 mg for 1900 h operation (Si was not yet quantified in post-test analyses), and to an evaporation rate of J_{Si} 1.5×10^{-10} $kg\,m^{-2}\,s^{-1}$, when considering all Si stemming from the BoP alloys.

However, this result far exceeds the expected evaporation rates [14,28–30]. Indeed, considering evaporation of Si-tetraoxyhydroxide from SiO_2, using thermodynamic date from Wuillemin [24] who extracted an equilibrium constant (Eq. (13)) from Jacobson and Opila's results [14,29,30], the equilibrium partial pressure of $Si(OH)_4$ under the cathode air-inlet conditions, can be calculated according to the following equation:

$$p_{Si(OH)_4} = K_{Si(OH)_4} \times p_{H_2O}^2 \quad (12)$$

$$\log K_{Si(OH)_4} = -2857.84 \times T^{-1} - 3.53 \quad (13)$$

which equals $p_{Si(OH)_4} = 2 \times 10^{-12}$atm. This would correspond to an evaporation rate of 7.3×10^{-15} $kg\,m^{-2}\,s^{-1}$. Therefore, Si contamination from Si-species is expected in other forms than $Si(OH)_4$.

Filtering the laboratory air did not reveal traces of Si that could stem from silicone oil and rubber or siloxane greases, as reported in literature [35,36]. On the other hand, atmospheric particular matter (PM) from environmental air, which is a complex mixture of elemental and organic carbon, ammonium, nitrates, sulfates, trace elements, water and mineral dust [37], might pass mechanical filtering. However, in this case, a maximum contribution of

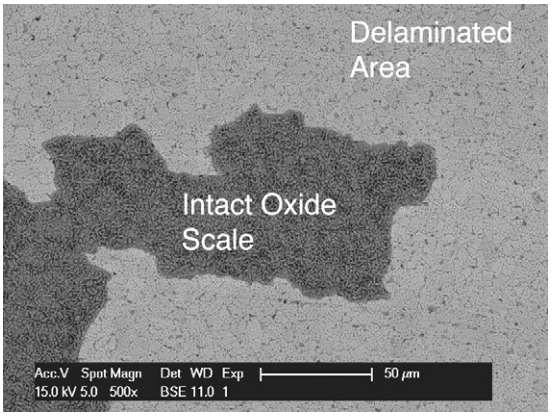

Fig. 8. High Si-concentrations in sub-scale layers fragilize alloy/sub-scale and sub-scale/scale interfaces. This low magnification SEM image presents an oxide scale (dark grey) that partially delaminated exposing Si-rich sub-scale surface (light grey).

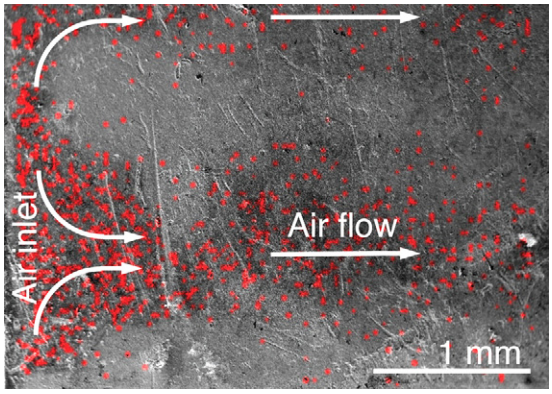

Fig. 9. Spatial distribution of Si observed by EDS on zirconia remnants after cathode dissolution in acid. The low magnification surface view shows Si to follow the airflow pattern (air-entry on the left).

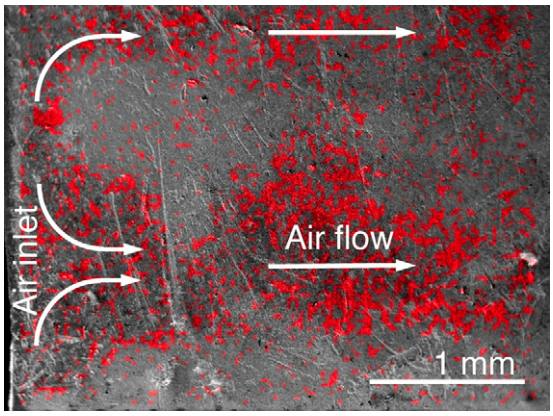

Fig. 10. When sulfur reacts within the CCL, LSC decomposes (Eq. (14)) into Co_3O_4. After dissolution of the cathode in acid, Co_3O_4 is observed in zirconia remnants and follows the pattern of the airflow, as shown by this EDS mapping, indicating the source of sulfur contamination to be located upstream of the cell.

about 1 $\mu g\,m^{-3}$ Si (calculated from mineral dust composition: Si = 1.89Al + 1.66Mg + 1.21K + 1.40Ca + 1.43Fe + 2.14Si) is expected [37].

Nevertheless, Si influences both electrolyte and electrode performance, limiting oxygen exchange reactions [6,32,35,36], as Si forms insulating amorphous low-melting eutectics with alkaline and alkaline rare-earth (RE) elements [14,28,34,38,39]. Rare-earth disilicates, in the form of $RESi_2O_5$ and $RESi_2O_7$, are found in the literature [14,39], including La-silicate [34] and Sr-silicate Sr_2SiO_4 [27]; on the other hand, formation of $ZrSiO_4$ is reported to be unfavorable under SOFC operation conditions [32].

Delaminations in the cathode, upon silicate formation, are expected because of differences in TECs [38]. However, TEC values for RE-disilicates are not available in the open literature [39].

Backhaus-Ricoult [31] suggests that the bulk Si impurity level in ceramic powders is sufficient to produce full coverage of an electrolyte surface with a monolayer of silica; in the present study, severe Si-contamination from exogenous sources was shown. Already small coverage of Si can hinder oxygen exchange on electrolyte surfaces, as the oxygen-sticking factor on cathode materials is low at SOFC operation temperatures [31]. The influence of Si in SOFC testing has to be considered, as its presence is ubiquitous [40]; different Si-contamination levels may be responsible for the disagreement in the literature related to the behavior of air side components.

Similar to the observation of Si-pollution within the cathode, the effect of sulfur on the latter is shown in Fig. 10. Sulfur reacts with LSC from the CCL, according to the following equation [1]:

$$6La_{0.5}Sr_{0.5}CoO_3 + 3SO_2 + 1/2O_2 \leftrightarrow 3SrSO_4 + Co_3O_4 + 3LaCoO_3 \quad (14)$$

where LSC decomposes into strontium sulfate $SrSO_4$, lanthanum-cobaltite $LaCoO_3$ (LC) and cobalt oxide Co_3O_4. The latter is observed in Fig. 10 and follows the airflow pattern, whereas the perovskites LSM, LSC and LC have been dissolved. The source of sulfur pollution was thus located upstream of the cell.

Moreover, the *in situ* hot air sampling experiment enabled to determine an amount of 6 $\mu g\,m^{-3}$ sulfur in the hot air flux; this would correspond to an accumulation of 14 mg sulfur in the cathode after 1900 h testing. Compressed air filtering revealed sulfur in combination with organic material, indicating the laboratory air to be the source of sulfur, conveying 12 ppb SO_2. Amounts around 10 ppb of SO_2 are typical for Swiss urban air (daily measured by the Swiss Office for the Environment FOEN) and is close to the amount of sulfur measured in this work.

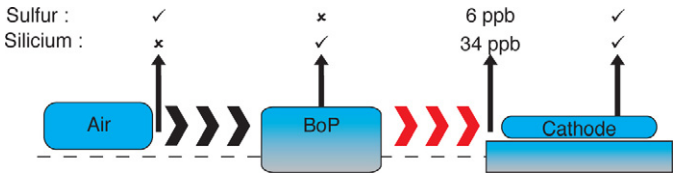

Fig. 11. Silicon and sulfur were revealed as air side contaminants in SOFC testing. Quantitative data was so far only given by the *in situ* hot air sampling analysis. The symbols indicate whether a contamination source was identified upstream the contamination accumulations in the cathode or not.

Fig. 11 summarizes analysis-locations where Si and sulfur were revealed as air side contamination. Additional air contaminants were measured at different analysis-locations including sodium, potassium and chlorine; these foreign elements were reported, as air side contaminants, in other studies [10,26]. Alkaline species were shown to act in degradation chain mechanisms on the air side, as they promote the formation of eutectics [3,4]. The laboratory air can convey inorganic salts, in particular by its water content, as the salts are absorbed to form aqueous solutions when the humidity in air reaches the deliquescence point [37]. As analyses on the compressed air showed only 5% RH, further studies are ongoing to access the sources of these pollutant species.

6. Conclusion

Severe air side contamination by pollutant species generated in system components, as well as supplied by external sources, was revealed in this study. Regarding Cr-contamination, it was shown that the BoP saturates the air with Cr-vapor species. Moreover, this concentration could be measured *in-situ* in the hot air flux, and was well correlated to Cr accumulations in a cell tested within the system.

SOFC components and button cells are often tested in inert setups where Cr-poisoning is avoided by the absence of BoP system parts. Even in such an approach, unexpected contamination sources are introduced; for instance, a thermocouple in proximity of the cathode was shown to be a source of Cr-poisoning [41].

However, different behaviors are observed for cells, short stacks and stacks; the most important difference is their thermal environment. SOFC testing in stack configuration is necessary especially when testing durability issues and longevity. In such conditions, air-side contamination stemming from BoP components as well as from the air itself was confirmed in the present work, emphasizing the priority of Cr reduction from BoP when Cr protection from MICs is adequate, as already stated in a previous study [2].

Protection, filtering and trapping are hence necessary features that have to be integrated in the design of SOFC test benches. Testing in an inert setup with the possibility to change a single BoP component at a time is another interesting option [26].

Finally, the analyses on air-filters answered the requested need of analyzing the compressed air [10]; such strategies are suggested to reduce the laboratory specific nature of SOFC component behavior, which is mainly due to impurities [6].

Acknowledgments

Financial support from the Swiss Federal Energy Office (Contract 153569, AccelenT), the European Commission (FP6 contract SES6-019875, Flame-SOFC), the Competence Center Energy and Mobility (CCEM-CH) in the framework of WoodGas-SOFC (Project 705028) and the swiss*electric* research project TREPGAS is gratefully acknowledged. Stéphane Thonney and Dr. Christophe Roussel (Section of Chemistry and Chemical Engineering/Institute of Chemical Sciences and Engineering/EPFL) are acknowledged for XRF

and AAS measurements. Many thanks to Dr. Anca Haiduc (Environmental Engineering Institute/School of Architecture, Civil and Environmental Engineering/EPFL) for the ICP-OES measurements.

References

[1] J.A. Schuler, Z. Wuillemin, A. Hessler-Wyser, J. Van herle, ECS Trans. 25 (2009) 2845–2852.
[2] Z. Wuillemin, A. Nakajo, A. Mueller, J.A. Schuler, S. Diethelm, J. Van herle, D. Favrat, ECS Trans. 25 (2009) 457–471.
[3] H. Yokokawa, T. Horita, K. Yamaji, H. Kishimoto, Y.P. Yiong, M.E. Brito, Proceedings of the 8th European SOFC Forum, vol. B1004, 2008, pp. 1–12.
[4] H. Yokokawa, H. Tu, B. Iwanschitz, A. Mai, J. Power Sources 182 (2008) 400–412.
[5] H. Yokokawa, T. Watanabe, A. Ueno, K. Hoshino, ECS Trans. 7 (2007) 133–140.
[6] M. Mogensen, K.V. Jensen, M.J. Jorgensen, S. Primdahl, Solid State Ionics 150 (2002) 123–129.
[7] R.R. Liu, S.H. Kim, Y. Shiratori, T. Oshima, K. Ito, K. Sasaki, ECS Trans. 25 (2009) 2859–2866.
[8] S. Tanagushi, M. Kadowaki, H. Kawamura, T. Yasuo, Y. Akiyama, Y. Miyake, T. Saitoh, J. Power Sources 55 (1995) 73–79.
[9] K. Gerdes, C. Johnson, J. Fuel Cell Sci. Technol. 6 (2009) 011018.
[10] A. Hagen, Y.L. Liu, R. Barfod, P.V. Hendriksen, J. Electrochem. Soc. 155 (2008) B1047–B1052.
[11] M. Koebel, M. Elsener, J. Chromatogr., A 689 (1995) 164–169.
[12] P. Kofstad, R. Bredesen, Solid State Ionics 52 (1992) 69–75.
[13] S.P.S. Badwal, R. Deller, K. Foger, Y. Ramprakash, J.P. Zhang, Solid State Ionics 99 (1997) 297–310.
[14] E.J. Opila, N.S. Jacobson, D.L. Myers, E.H. Copland, J. Miner. Met. Mater. Soc. 58 (2006) 22–28.
[15] D.J. Young, B.A. Pint, Oxid. Met. 66 (2006) 137–153.
[16] C. Wagner, Atom Movements, American Society of Metals, Cleveland, OH, 1951.
[17] K. Hauffe, Oxidation of Metals, Plenum Press, New York, 1965.
[18] Z. Yang, K.S. Weil, D.M. Paxton, J.W. Stevenson, J. Electrochem. Soc. 150 (2003) A1188–A1201.
[19] C.S. Tedmon, J. Electrochem. Soc. 113 (1966) 766–768.
[20] B.B. Ebbinghaus, Combust. Flame 93 (1993) 119–137.
[21] C. Gindorf, L. Singheiser, K. Hilpert, J. Phys. Chem. Solids 66 (2005) 384–387.
[22] M. Stanislowski, E. Wessel, T. Markus, L. Singheiser, W.J. Quadakkers, Solid State Ionics 179 (2008) 2406–2415.
[23] M. Stanislowski, E. Wessel, K. Hilpert, T. Markus, L. Singheiser, J. Electrochem. Soc. 154 (2007) A295–A306.
[24] Z. Wuillemin, Experimental and modeling investigations on local performance and local degradation in solid oxide fuel cells, EPFL Thesis 4525 (2009) 255–262.
[25] M. Stanislowski, J. Froizheim, L. Niewolak, W.J. Quadakkers, K. Hilpert, T. Markus, L. Singheiser, J. Power Sources 164 (2007) 578–589.
[26] N.H. Menzler, I. Vinke, H. Lippert, ECS Trans. 25 (2009) 2899–2908.
[27] R. Bauer, M. Baccalaro, L.P.H. Jeurgens, M. Pohl, E.J. Mittemeijer, Oxid. Met. 69 (2008) 265–285.
[28] I. Kaus, K. Wiik, M. Dahle, M. Brustad, S. Aasland, J. Eur. Ceram. Soc. 27 (2007) 4509–4514.
[29] E.J. Opila, D.S. Fox, N.S. Jacobson, J. Am. Ceram. Soc. 80 (1997) 1009–1012.
[30] N.S. Jacobson, E.J. Opila, D.L. Myers, E.H. Copland, J. Chem. Thermodyn. 37 (2005) 1130–1137.
[31] M. Backhaus-Ricoult, Solid State Sci. 10 (2008) 670–688.
[32] J.-H. Lee, Monatsh. Chem. 140 (2009) 1081–1094.
[33] B.C.H. Steele, Solid State Ionics 134 (2000) 3–20.
[34] D. Kuscner, J. Holk, M. Hrovat, S. Bernik, Z. Samardzija, D. Kolar, Solid State Ionics 78 (1995) 79–85.
[35] M. de Ridder, A.G.J. Vervoort, R.G. van Welzenis, H.H. Brongersma, Solid State Ionics 156 (2003) 255–262.
[36] M.M. Viitanen, R.G. van Welzenis, H.H. Brongersma, F.P.F. van Berkel, Solid State Ionics 150 (2002) 223–228.
[37] C. Hueglin, R. Gahrig, U. Baltensperger, M. Gysel, C. Monn, H. Vonmont, Atmos. Environ. 39 (2005) 637–651.
[38] S.B. Adler, Chem. Rev. 104 (2004) 4791–4843.
[39] E.J. Opila, R.C. Robinson, D.S. Fox, R.A. Wenglarz, M.K. Ferber, J. Am. Ceram. Soc. 86 (2003) 1262–1273.
[40] J.-M. Bae, B.C.H. Steele, Solid State Ionics 106 (1998) 247–253.
[41] D. Oh, E. Armstrong, D. Jung, C. Kan, E. Wachsman, ECS Trans. 25 (2009) 2871–2879.